A CPFEM based theoretical analysis of strains resolved by the microstructural feature tracking method

R Li, Romain Quey, Y Zhang, M Kobayashi, Jette Oddershede, D Juul Jensen

A CPFEM based theoretical analysis of strains resolved by the microstructural feature tracking method

R Li[1*], R Quey[2], Y Zhang[1], M Kobayashi[3], J Oddershede[4] and D Juul Jensen[1]

[1] Department of Civil and Mechanical Engineering, Technical University of Denmark, 2800 Kgs. Lyngby, Denmark
[2] Mines Saint-Etienne, Univ Lyon, CNRS, UMR 5307 LGF, F - 42023 Saint-Etienne, France
[3] Department of Mechanical Engineering, Toyohashi University of Technology, Toyohashi, Aichi 441-8580, Japan
[4] Xnovo Technology ApS, DK-4600 Køge, Denmark

*E-mail: rulia@dtu.dk

Abstract. In this work, it is investigated how grain boundaries influence the local strain determination by the microstructural feature tracking (MFT) algorithm. In this method, tetrahedra are used as the strain calculation unit. We apply the MFT processing procedure on data obtained by a crystal plasticity finite element modeling (CPFEM) simulation to explore the uncertainties in the calculated strains caused by grain boundaries. Effects of tetrahedron types and radius ratios are discussed.

1. Introduction

The strain distribution that develops in polycrystalline materials during plastic deformation is important for understanding their mechanical properties. It has been demonstrated that the microstructural feature tracking (MFT) method is capable of mapping the internal local strain fields within particle-contained bulk metals [1,2], from which the relationships between microstructures and local deformation heterogeneities can be elucidated.

The accuracy of local strain determination based on the MFT method has already been evaluated in terms of particle characteristics in [3], but other factors are still worth investigating. A particular one is related to the spatial resolution of the method and how strong deformation heterogeneities caused by microstructure discontinuities, like grain boundaries, influence the estimation of grain-averaged strains. Previous studies of deformed microstructures have revealed that these discontinuities can cause stress/strain concentrations due to incompatibilities in strain components of neighboring grains [4,5].

The MFT method typically uses a relatively sparse distribution of particles in the microstructure. The particles serve as vertices of the strain analysis tetrahedral units, some of which are distributed within grains, but others cross grain boundaries and effectively cover several grains. The possible large local strain variations induced by boundaries may be smeared out in the MFT analysis. How such strain smearing may influence the MFT results needs to be clarified.

This paper aims to explore the effects of grain boundaries on MFT-measured strains. Instead of using actual experimental data, and to isolate the effect of the spatial resolution associated to the density of the particle distribution, we use a CPFEM simulation to generate model data. Based on the ground truth strain dataset computed via simulation, the effects of the different tetrahedron types and radius ratios on the calculated strains are investigated.

2. Simulation details and analysis method

2.1 CPFEM simulation

The simulation is based on the actual morphology and orientation of an Al-4mass%Cu alloy sample characterized by laboratory-based X-ray diffraction contrast tomography (LabDCT) [3,6]. Figure 1a shows the grain structure of the gauge section of the undeformed sample, which is typical of a well-annealed polycrystalline sample with an average grain size of ~80 μm and a weak texture. The simulation mesh was generated from the experimental data following the procedure detailed in Refs. [7] and [8] and implemented in Neper [8], according to which the grain structure was first approximated by its nearest convex-cell geometry. The resulting tessellation was then meshed into hundreds of elements per grain, leading to a total of 2,673,622 elements. Figure 1d shows the mesh. The FEPX code was employed to simulate the elastoplastic deformation of the virtual polycrystalline aggregates [9]. Tensile loads were applied along the z-axis.

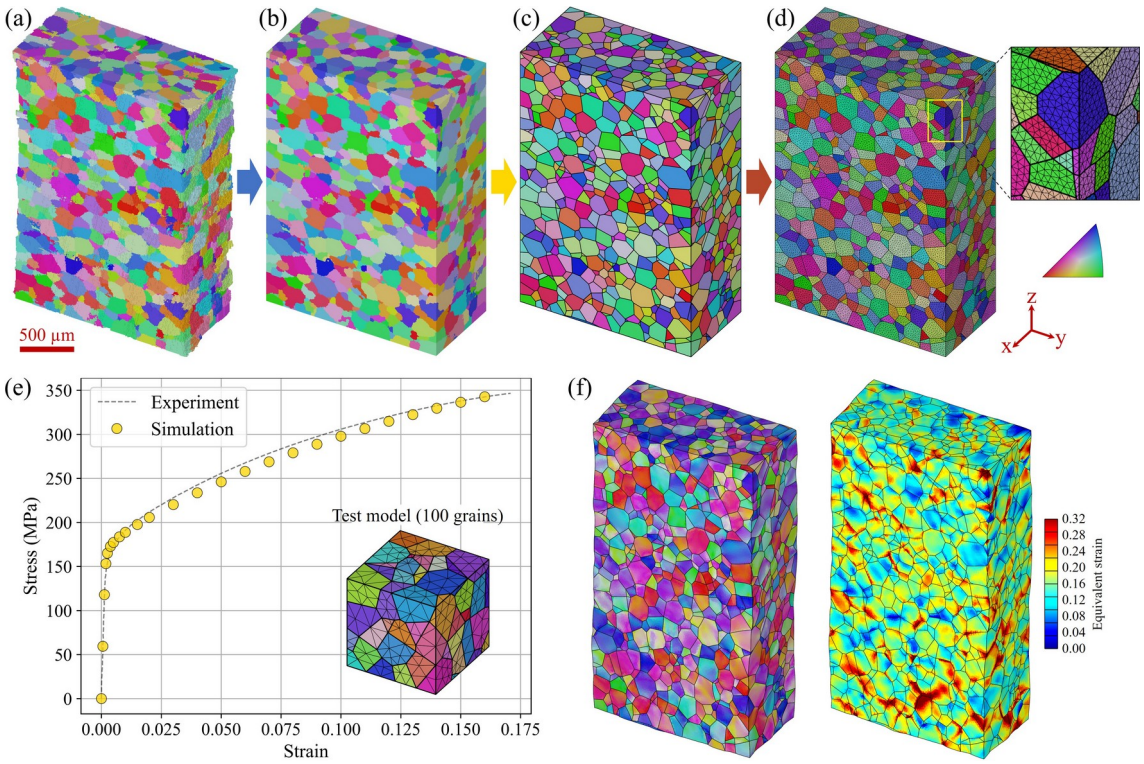

Figure 1. Model configurations. (a) LabDCT measurement, (b) cropped volume, (c) nearest convex-cell approximation, and (d) mesh. (e) Experimental and simulated stress-strain curves. (f) Orientation and equivalent strain maps of the 16% tensile deformed sample.

The material is described via an elastic and a rate-dependent plastic response. The stress (σ) is related to the elastic strain (ε) via Hooke's law: $\sigma = \mathbf{C}\varepsilon$, where $\mathbf{C}$ is the stiffness tensor, defined by the input parameters C_{11}, C_{12}, and C_{44} for cubic materials. The slip kinetics, assumed to be identical for all

slip systems, has the form of $\dot{\gamma}^{\alpha}=\dot{\gamma}_0\left(\frac{\left|\tau^{\alpha}\right|}{g^{\alpha}}\right)^{\frac{1}{m}}sgn\left(\tau^{\alpha}\right)$, where $\dot{\gamma}^{\alpha}$ is the shear strain rate of the slip system α, $\dot{\gamma}_0$ is the fixed-rate strain rate scaling coefficient, g^{α} and τ_{α} are the critical resolved shear stress (CRSS) and current resolved shear stress of slip system α, and m is the rate sensitivity exponent. The slip hardening ($\dot{g}$) is modeled by $\dot{g}^{\alpha}=h_0\left(\frac{g_s\left(\dot{\gamma}\right)-g^{\alpha}}{g_s\left(\dot{\gamma}\right)-g_0}\right)^{n}\dot{\gamma}$, where g_0 and $g_s\left(\dot{\gamma}\right)$ are the starting and saturation CRSS of slip system α, h_0 is the fixed-state hardening rate scaling coefficient, and n is the non-linear Voce hardening exponent. The slip system saturation strength is calculated at a given state as $g_s\left(\dot{\gamma}\right)=g_{s0}\left(\frac{\dot{\gamma}}{\dot{\gamma}_{s0}}\right)^{m'}$, where g_{s0} is the initial slip system saturation strength, m' is the saturation strength rate scaling exponent, $\dot{\gamma}_{s0}$ is the initial saturation slip system shear rate. $\dot{\gamma}$ is calculated as $\dot{\gamma}=\sum_{\alpha}\left|\dot{\gamma}^{\alpha}\right|g_{s0}\left(\frac{\dot{\gamma}}{\dot{\gamma}_{s0}}\right)^{m'}$. In order to calibrate the crystal-scale material constants, we use a smaller model containing 100 grains (the inset of figure 1e) and fit the measured macroscopic stress. The resulting constants are provided in table 1, and the experimental and simulated stress-strain curves are plotted in figure 1e. Figure 1f shows the simulated orientation and equivalent strain maps of the 16% tensile deformed sample, featuring typical orientation spreading and an inhomogeneous strain distribution.

Table 1. Single-crystal elastic constants (aluminum) and elasto-viscoplastic model constants used in the simulation.

C_{11}, GPa	C_{12}, GPa	C_{44}, GPa	h_0, MPa	g_0, MPa	g_{s0}, MPa	m	m'	$\dot{\gamma}_0$, 1/s	$\dot{\gamma}_{s0}$, 1/s
107.3	60.9	28.32	300.0	85.0	240.0	0.05	0.005	1.0	5×10^{10}

2.2 MFT analysis

We randomly selected 15,000 points in the virtual polycrystal aggregates to serve as virtual marker particles (corresponding to an average of 4 markers per grain). Following the MFT method, tetrahedra were generated from these marker particles by Delaunay triangulation [10], leading to a tetrahedral mesh where particles represent nodes (the tetrahedron "vertices") covering a total of 99,431 tetrahedra (i.e., about 1/27 of those for CPFEM). The local strains were then evaluated within the tetrahedra from the relative displacements of the vertices during straining by the MFT method as detailed in [1]. The von Mises equivalent strain, ε_{eq}, referred to as "strain" in the following, is defined as $\varepsilon_{eq}=\sqrt{\frac{2}{3}\left(\varepsilon_{xx}^2+\varepsilon_{yy}^2+\varepsilon_{zz}^2\right)+\frac{1}{3}\left(\varepsilon_{yz}^2+\varepsilon_{xz}^2+\varepsilon_{xy}^2\right)}$. The MFT strains and the effective CPFEM strains were then compared. The MFT grain strains, defined as the volume-weighted average strain over tetrahedra or parts of tetrahedra within a grain, were also considered. Similarly, a CPFEM grain strain was defined as the volume-weighted average strain over all elements within a grain.

We classified the strain tetrahedra into five types, depending on their positions relative to grains and grain boundaries. As illustrated in figure 2a, "Tetrahedron-4" represents tetrahedra for which all vertices are located inside the same grain. "Tetrahedron-31 and -22" represent tetrahedra whose vertices are located in two connected grains, which are therefore crossing a grain boundary. Finally, "Tetrahedron-211 and -1111" represent tetrahedra whose vertices are located in 3 or 4 grains, respectively, and which are therefore containing a grain junction. Following this notation, each digit corresponds to the number of vertices inside distinct grains.

The generation of tetrahedral elements from marker particles by Delaunay triangulation often leads to a certain amount of ill-shaped tetrahedra, which may also influence the strain determination. Thus, in the following analysis, we introduce the tetrahedron radius ratio (r) to further classify the tetrahedra. As described in figure 2b, r is defined as $3Ri/Ro$, where Ri and Ro are the radii of the inscribed and circumscribed spheres of a tetrahedron, respectively. The ratio ranges between 0 and 1, and a higher value implies a better quality of the tetrahedron. Figure 2c shows the number of tetrahedra as a function of r, highlighting the existence of some low-quality tetrahedra with extremely low r for the present virtual dataset.

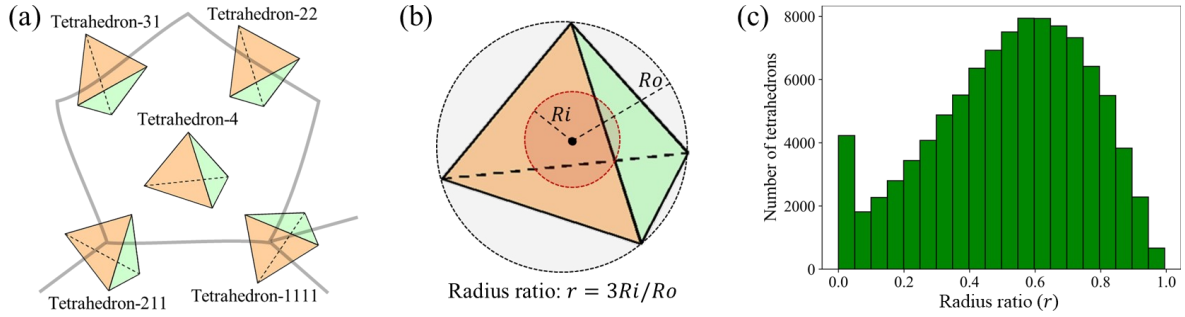

Figure 2. (a) Tetrahedron classification. (b) Tetrahedron radius ratio (r). (c) Frequency distribution of the radius ratios.

3. Results and discussion

We analyzed first MFT tetrahedron strains as a function of tetrahedron type. Since the 'ground truth' strain distribution within each MFT tetrahedron can be acquired from the CPFEM strains within the much refined finite element volumes, a quantitative analysis of the representativeness of the MFT tetrahedron strain can be performed. We therefore first performed the analysis based on the CPFEM strains and then examined the MFT grain strains, based on which suggestions to further improve the accuracy of MFT grain are given.

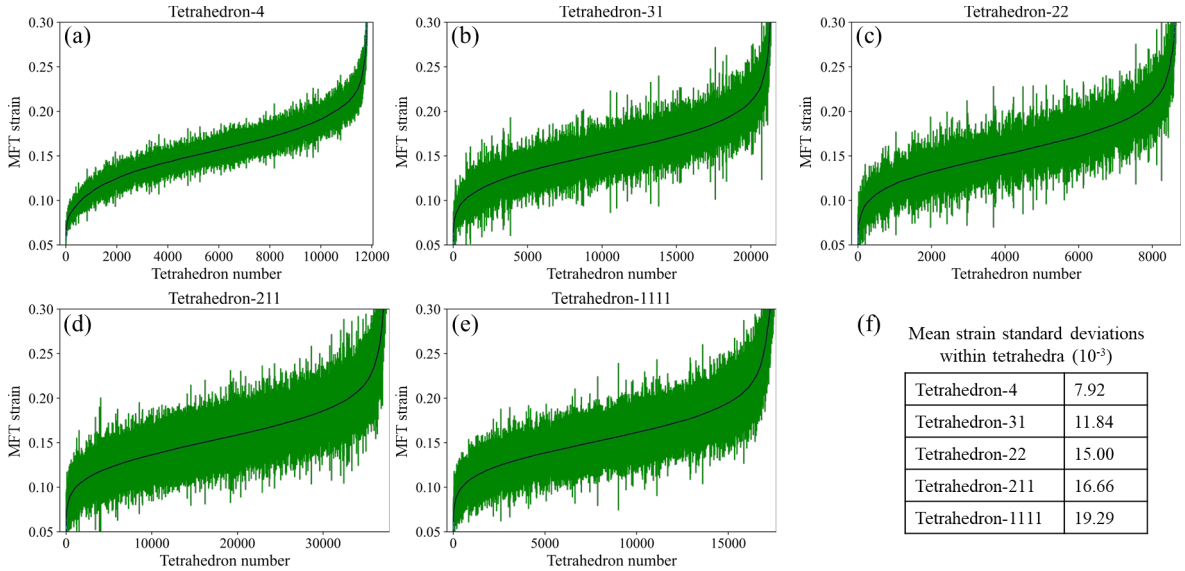

Tetrahedron-4	7.92
Tetrahedron-31	11.84
Tetrahedron-22	15.00
Tetrahedron-211	16.66
Tetrahedron-1111	19.29

Figure 3. MFT strains for different types of tetrahedra. (a) Tetrahedron-4. (b) Tetrahedron-31. (c) Tetrahedron-22. (d) Tetrahedron-211. (e) Tetrahedron-1111. The strain standard deviation for each tetrahedron is shown in green lines. The mean strain standard deviation data for each type of tetrahedra are listed in (f).

Figure 3 shows the MFT strains for different types of tetrahedra. For clarity, strains of the tetrahedra are plotted by increasing strain magnitude as shown by the black line, and the strain standard deviation for each tetrahedron is shown as green lines. Significantly smaller strain standard deviations are noticed in Tetrahedron-4 (figure 3a) than for the other ones (figure 3b-e), see also figure 3f, suggesting that the local strain distributions in Tetrahedron-4 are generally more homogeneous than in other tetrahedra types. The result is understandable because all the other types of tetrahedra contain boundaries or boundary junctions (figure 2a), where the parts belonging to different grains may have significantly different strains, therefore giving a greater probability of recording highly heterogeneous strains.

As the calculation of the MFT grain strain is based on the strains of tetrahedra within or connected to the specific grain, the above-mentioned effects of tetrahedron type may lead to uncertainties in MFT grain strain. To evaluate such uncertainties, the MFT grain strain and CPFEM grain strain for each grain are compared. Furthermore, by selecting different tetrahedra used for MFT grain strain calculation, suggestions on how to optimize such data processing are given.

To maximize accuracy, only grains containing more than 100 vertices are considered. The grain strains calculated by MFT are plotted against those calculated by CPFEM for different r ranges: $r > 0.0$, $r > 0.1$, and $r > 0.5$, in figure 4a, where all tetrahedra are considered. The degree of deviation of the data spots from the identity line indicates how much the MFT grain strains differ from the CPFEM grain strains. As seen from the figure, there are many significantly deviating data points in the $r > 0.0$ plot, but not so many in the $r > 0.1$ and $r > 0.5$ plots. The apparent decrease in the number of deviating grains indicates that the ill-shaped tetrahedra, having lower r values (mostly lower than 0.1), are responsible for the erroneously MFT calculated grain strains. That the strain data are being distributed around lines with slopes significantly lower than 1, suggests that the strain heterogeneities are underestimated by MFT, which may be explained from the averaging effect of boundary-crossing tetrahedra. This is analyzed in the following.

The plots of figure 4b are drawn in the same manner as figure 4a, but for Tetrahedron-4 only. Only large grains, which contain more than 25 Tetrahedron-4 types, are considered. The results clearly show that, after excluding the averaging effect of boundary-crossing tetrahedra, the MFT grain strains are in better agreement with the CPFEM grain strains. This indicates that, for those large grains, the strain averaged over all Tetrahedron-4 is more representative of the effective strain than the MFT strain averaged over all tetrahedra.

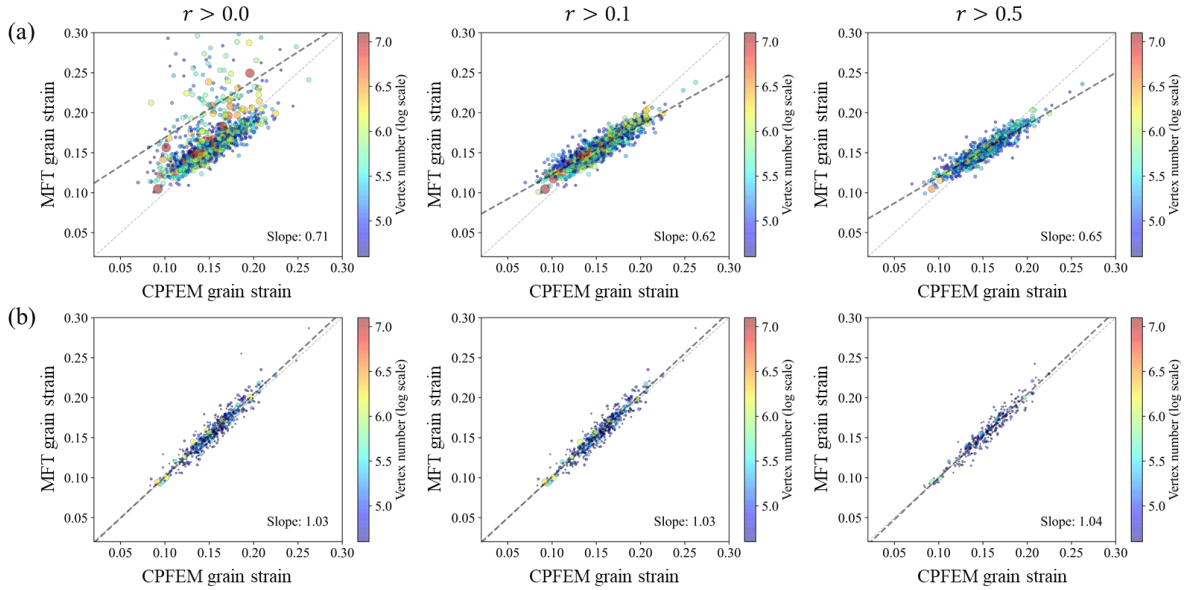

Figure 4. MFT grain strain versus CPFEM grain strain with different r ranges, *i.e.*, $r > 0.0$, $r > 0.1$, and $r > 0.5$. (a) Calculated using all tetrahedra. (b) Calculated using Tetrahedron-4 only. The black dashed line and light dashed line are the linear fit of the data spots and the identity line, respectively.

4. Conclusions

The data processing procedure of the MFT method was evaluated using reference results obtained by CPFEM simulations. The influence of the type and radius ratio of the MFT tetrahedral elements on the computed strains was analyzed. It was found that the strain calculated from the tetrahedra for which all vertices are located inside the same grain is more representative of the local strain than the strain computed using all tetrahedra, including those overlapping grain boundaries. In the MFT method, the strain heterogeneity of boundary-crossing tetrahedra tends to be underestimated. It was also shown that significant uncertainty is induced in the MFT strain calculations when low radius ratio tetrahedra are used. In short, the analysis highlighted the pros and cons of the MFT method for strain measurements, and the results can be used for optimizing the MFT data processing. Additionally, the results may be of value to improve also other methods such as digital image correlation and digital volume correlation.

Acknowledgments

The financial support from the European Research Council (ERC) under the European Union's Horizon 2020 research and innovation programme (M4D-grant agreement No. 788567) is gratefully acknowledged.

References

[1] Toda H, Minami K, Koyama K, Ichitani K, Kobayashi M, Uesugi K and Suzuki Y 2009 Healing behavior of preexisting hydrogen micropores in aluminum alloys during plastic deformation *Acta Mater.* **57** 4391–403

[2] Kobayashi M, Miura H and Toda H 2015 Non-destructive and three-dimensional measurement of local strain development during tensile deformation in an aluminium alloy *IOP Conf. Ser.: Mater. Sci. Eng.* **89** 012030

[3] Kobayashi M, Zhang Y, Ishikawa H, Sun J, Oddershede J, Juul Jensen D and Miura H 2021 Investigation of relationships between grain structure and inhomogeneous deformation by means of laboratory-based multimodal X-ray tomography: strain accuracy analysis *Exp. Mech.*

[4] Bieler T R, Eisenlohr P, Zhang C, Phukan H J and Crimp M A 2014 Grain boundaries and interfaces in slip transfer *Curr. Opin. Solid State Mater. Sci.* **18** 212–26

[5] Kocks U F and Canova G R 1981 How many slip systems, and which? *Deformation of Polycrystals: Mechanisms and Microstructures. 2 nd Riso Int. Symposium on Metallurgy and Materials Science* 35–44

[6] Kobayashi M, Zhang Y, Ishikawa H, Sun J, Oddershede J, Jensen D J and Miura H 2021 Relationships between 3D grain structure and local inhomogeneous deformation: A laboratory-based multimodal X-ray tomography investigation *submitted to Acta Materialia for consideration*

[7] Quey R and Renversade L 2018 Optimal polyhedral description of 3D polycrystals: Method and application to statistical and synchrotron X-ray diffraction data *Comput. Methods Appl. Mech. Eng.* **330** 308–33

[8] Quey R, Dawson P R and Barbe F 2011 Large-scale 3D random polycrystals for the finite element method: Generation, meshing and remeshing *Comput. Methods Appl. Mech. Eng.* **200** 1729–45

[9] Dawson P R and Boyce D E 2015 FEpX--Finite element polycrystals: Theory, finite element formulation, numerical implementation and illustrative examples *arXiv:1504.03296*
[10] Barber C B, Dobkin D P and Huhdanpaa H 1996 The quickhull algorithm for convex hulls *ACM Trans. Math. Softw.* **22** 469–83